

Shear wave imaging from traffic noise using seismic interferometry by cross-coherence

Norimitsu Nakata¹, Roel Snieder², Takeshi Tsuji¹, Ken Lerner², and Toshifumi Matsuoka¹

ABSTRACT

We apply the cross-coherence method to the seismic interferometry of traffic noise, which originates from roads and railways, to retrieve both body waves and surface-waves. Our preferred algorithm in the presence of highly variable and strong additive random noise uses cross-coherence, which uses normalization by the spectral amplitude of each of the traces, rather than crosscorrelation or deconvolution. This normalization suppresses the influence of additive noise and overcomes problems resulting from amplitude variations among input traces. By using only the phase information and ignoring amplitude information, the method effectively removes the source signature from the extracted response and yields a stable structural reconstruction even in the presence of strong noise. This algorithm is particularly effective where the relative amplitude among the original traces is highly variable from trace to trace. We use the extracted, reflected shear waves from the traffic noise data to construct a stacked and migrated image, and we use the extracted surface-waves (Love waves) to estimate the shear velocity as a function of depth. This profile agrees well with the interval velocity obtained from the normal moveout of the reflected shear waves constructed by seismic interferometry. These results are useful in a wide range of situations applicable to both geophysics and civil engineering.

INTRODUCTION

The main purpose of seismic interferometry is to construct a Green's function between two geophones, hydrophones, or accelerometers through the data processing of signals generated by earthquakes, microtremors, cultural noise, or artificial seismic

sources. Green's function extraction can be derived from normal modes (Lobkis and Weaver, 2001), representation theorems (Wapenaar, 2004; Wapenaar and Fokkema, 2006), the principle of time reversal (Roux and Fink, 2003), and stationary phase analysis (Snieder et al., 2006). After such processing, one geophone serves as a (virtual) source for waves recorded by other receivers, which leads to a pseudoshot gather for many receivers, without using an active source.

Although the first application of seismic interferometry was based on cross-coherence (Aki, 1957), the first applied algorithm in seismic interferometry that found wide application is based on crosscorrelation (Claerbout, 1968; Wapenaar, 2003; Bakulin and Calvert, 2004; Schuster et al., 2004). Another proposed algorithm is based on deconvolution. In this method, the source signal is removed by means of spectral division. The mathematical theory of deconvolution interferometry has been derived by Vasconcelos and Snieder (2008a), and the method has been applied to field data (Snieder and Şafak, 2006; Vasconcelos and Snieder, 2008b; Vasconcelos et al., 2008). A multidimensional deconvolution method has been formulated for seismic interferometry (Wapenaar et al., 2008a, 2008b).

The various methods have both advantages and disadvantages (Table 1 of Snieder et al., 2009). Crosscorrelation, for example, is stable but needs estimation of the power spectrum of the noise source, and deconvolution is potentially unstable and, thus, needs regularization, but this method does not require estimation of the source spectrum. We should choose the method that best suits the data; to date, however, it has not been clear how these different methods behave when applied to data contaminated with highly variable and strong additive noise.

In this study we analyze the use of cross-coherence. This approach, used in seismology and engineering (e.g., Aki, 1957; Bendat and Piersol, 2000; Chávez-García and Luzón, 2005), calculates the crosscorrelation of traces normalized by their spectral amplitudes in the frequency-domain. Thus, the method uses the phase of each trace,

Manuscript received by the Editor 21 June 2010; revised manuscript received 25 June 2011; published online 9 January 2012.

¹Kyoto University, Department of Urban Management, Kyoto, Japan. E-mail: n_nakata@earth.kumst.kyoto-u.ac.jp; tsuji@earth.kumst.kyoto-u.ac.jp; matsuoka@earth.kumst.kyoto-u.ac.jp.

²Colorado School of Mines, Department of Geophysics, Golden, Colorado, USA. E-mail: nnakata@mines.edu; rsnieder@mines.edu; kenlerner@gmail.com.

© 2012 Society of Exploration Geophysicists. All rights reserved.

ignoring amplitude information, for suppressing the influence of additive noise and handling irregular input amplitudes. Bensen et al. (2007) show examples of normalization techniques applied in seismic interferometry.

Extracting surface-waves from the crosscorrelation of ambient noise is by now an established technique (e.g., Campillo and Paul, 2003; Shapiro et al., 2005). In contrast, the extraction of body waves has proven to be much more difficult. Extracting body waves by crosscorrelation has, however, been accomplished in some studies. Examples include the extraction of P-waves using distributed sources (e.g., Roux et al., 2005; Hohl and Mateeva, 2006; Draganov et al., 2007; Gerstoft et al., 2008; Draganov et al., 2009; Zhang et al., 2009) and of S-waves using localized noise sources (e.g., O'Connell, 2007; Miyazawa et al., 2008). This paper presents data processing of field data dominated by strong and highly variable traffic noise, as well as incoherent additive noise. We first present the basic equations of crosscorrelation, deconvolution, and cross-coherence interferometry. We further demonstrate the merits of cross-coherence interferometry applied to traffic noise data for the retrieval of surface-waves and reflected shear waves. Because the interferometry is based on the transverse horizontal component, the extracted surface-waves consist of Love waves, and the extracted body waves are mostly SH waves. Finally, we explain why the cross-coherence is particularly suitable to extract the approximated Green's function from this type of noisy data.

EQUATIONS OF INTERFEROMETRY

Consider the wavefield $u(r, s)$ excited at s and received at r . In this work we use a frequency-domain formulation for all data processing. Ignoring additive noise, the wavefield can be described as the multiplication of a source wavelet and a Green's function

$$u(r, s) = W(s)G(r, s), \quad (1)$$

where $W(s)$ is the source wavelet and $G(r, s)$ is the Green's function.

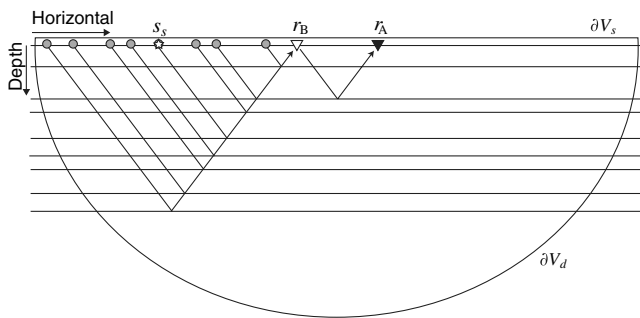


Figure 1. Stationary points of a body wave propagating between two receivers (r_A and r_B) from multiples reflected from different interfaces. The white triangle (r_B) denotes a receiver that acts as a pseudosource. Surfaces ∂V_s and ∂V_d represent the earth's free surface and an arbitrarily shaped surface, which together form a closed surface. The wave radiated by the pseudosource at r_B is reflected by a particular reflector, and then is recorded by a receiver marked with the black triangle (r_A). Gray circles denote stationary source locations for multiples that first reflect off layers on the left, and then propagate between the receivers marked by triangles. If a noise source (e.g. the white star) is close to one of the stationary points (s_s), we obtain the reflected wave propagating from r_B to r_A .

Crosscorrelation and deconvolution

Let us first review the crosscorrelation and deconvolution methods (Snieder et al., 2006; Vasconcelos and Snieder, 2008a) to compare them with the cross-coherence method. The crosscorrelation of wavefields recorded at locations r_A and r_B is

$$C_{AB} = u(r_A, s)u^*(r_B, s) = |W(s)|^2 G(r_A, s)G^*(r_B, s), \quad (2)$$

where the asterisk denotes a complex conjugate. Integrating this equation over a closed surface ∂V , which consists of the earth's surface (∂V_s in Figure 1) and an arbitrarily shaped surface at depth (∂V_d in Figure 1), gives for uncorrelated sources with a constant power spectrum (Wapenaar and Fokkema, 2006),

$$\oint_{\partial V} C_{AB} ds = \langle |W(s)|^2 \rangle \oint_{\partial V} G(r_A, s)G^*(r_B, s) ds, \quad (3)$$

where $\langle |W(s)|^2 \rangle$ is the average of the power spectra for the source wavelets. Because the integral $\oint_{\partial V} G(r_A, s)G^*(r_B, s) ds$ in equation 3 is proportional to $G(r_A, r_B)$ (Wapenaar and Fokkema, 2006), this gives, up to a multiplicative constant, the approximate Green's function between the two receivers. The retrieved estimate of the Green's function is not exact because it assumes that the waves propagate perpendicular to ∂V (Wapenaar and Fokkema, 2006). In reality, the waves may propagate at an angle through ∂V ; ignoring this renders the amplitude unreliable, but the phase is still correct.

Even though theory requires sources all over ∂V , the extracted Green's function is mostly determined by sources at stationary phase locations (Snieder, 2004; Snieder et al., 2006). These sources launch waves that propagate to one receiver, and then continue to the other receiver (Wapenaar et al., 2010). An example is shown in Figure 1, where a wave travels from a stationary source location s_s via receiver r_B to receiver r_A . For each peg-leg multiple, such a stationary source point exists (Figure 1), which leads to a multitude of stationary source points at the earth's surface.

The basic equation of deconvolution interferometry is

$$D_{AB} = \frac{u(r_A, s)}{u(r_B, s)} = \frac{G(r_A, s)}{G(r_B, s)} = \frac{G(r_A, s)G^*(r_B, s)}{|G(r_B, s)|^2}. \quad (4)$$

Deconvolution removes the influence of the source wavelet $W(s)$. Because of the absolute value in the denominator, the phase of D_{AB} is determined by the numerator $G(r_A, s)G^*(r_B, s)$ in the last term of equation 4; hence, the deconvolution gives the same phase as the crosscorrelation method (equation 2). The deconvolution method can also be used to extract the impulse response (Vasconcelos and Snieder, 2008a) when integrating over sources located on a closed surface ∂V . Because of the spectral division, the result is independent of the source signature. The method, thus, can deal with data generated by long and complicated source signals.

Cross-coherence

The cross-coherence H_{AB} is defined in the frequency-domain as

$$H_{AB} = \frac{u(r_A, s)u^*(r_B, s)}{|u(r_A, s)||u(r_B, s)|}. \quad (5)$$

The numerator of equation 5 is the same as the product in the expression for crosscorrelation (equation 2), and the denominator is the product of the amplitude spectra of the waveforms. This equation indicates that while the phase information is used, the amplitude information is discarded. Because the amplitude is, in practice, prone to inaccuracies, e.g., as a result of the difference of sensitivity among receivers or the variable orientation of receivers, the use of this equation is expected to retrieve more robust information than either crosscorrelation or deconvolution. We can rewrite equation 5 as

$$H_{AB} = \frac{G(r_A, s)G^*(r_B, s)}{|G(r_A, s)||G(r_B, s)|} \quad (6)$$

because cross-coherence cancels the source wavelet term $W(s)$ by division, as does deconvolution. Integrating equation 6 over a closed surface ∂V containing all sources gives

$$\oint_{\partial V} H_{AB} ds = \oint_{\partial V} \frac{G(r_A, s)G^*(r_B, s)}{|G(r_A, s)||G(r_B, s)|} ds; \quad (7)$$

hence, it provides the phase of the approximated Green's function between two receivers, but the amplitude is not preserved in this cross-coherence approach (Prieto et al., 2009). To clarify the characteristics of each approach, Nakata (2010) shows Taylor expansions of equations 2, 4, and 5 for small-amplitude scattered waves.

When $r_A = r_B$ in equations 5–7, the right-hand side is equal to 1, which corresponds to the Dirac delta function $\delta(t)$ in the time domain. This means that the field extracted by cross-coherence satisfies a so-called *clamped boundary condition* at r_B ; the same boundary condition occurs in deconvolution interferometry (Vasconcelos and Snieder, 2008a; Snieder et al., 2009) but not in crosscorrelation interferometry. In Figure 1, when we put r_A at the same point as r_B , the receiver point (equal to the pseudosource point) satisfies the clamped boundary condition in the sense that the retrieved wavefield vanishes for $t \neq 0$ as $r_A \rightarrow r_B$ (Vasconcelos and Snieder, 2008a).

In the deconvolution approach shown here, some level of white noise has to be added to prevent numerical instability. If we choose a regularization parameter that is too large, the regularized deconvolution reduces to crosscorrelation. If, however, the regularization parameter is too small, the deconvolution is unstable. Although instability also occurs in cross-coherence, in practice, we can choose a much smaller regularization parameter, because the numerator and denominator are both small when the spectral amplitude is small.

FIELD DATA PROCESSING

Data acquisition and pseudoshot gathers

We apply the cross-coherence method to traffic noise data acquired in Gunma, Japan. An aerial photograph of the observation site is shown in Figure 2a. The survey line (blue line in Figure 2a) is

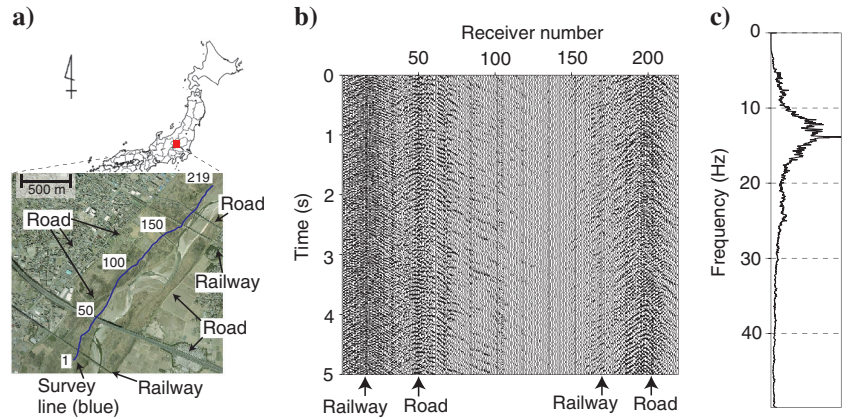


Figure 2. (a) Location of the survey line for observing traffic noise at Gunma, Japan: the line parallels a river and crosses some roads and train lines. (b) Observed noise record. The receiver number increases from south to north. (c) Power spectrum of the data in panel (b).

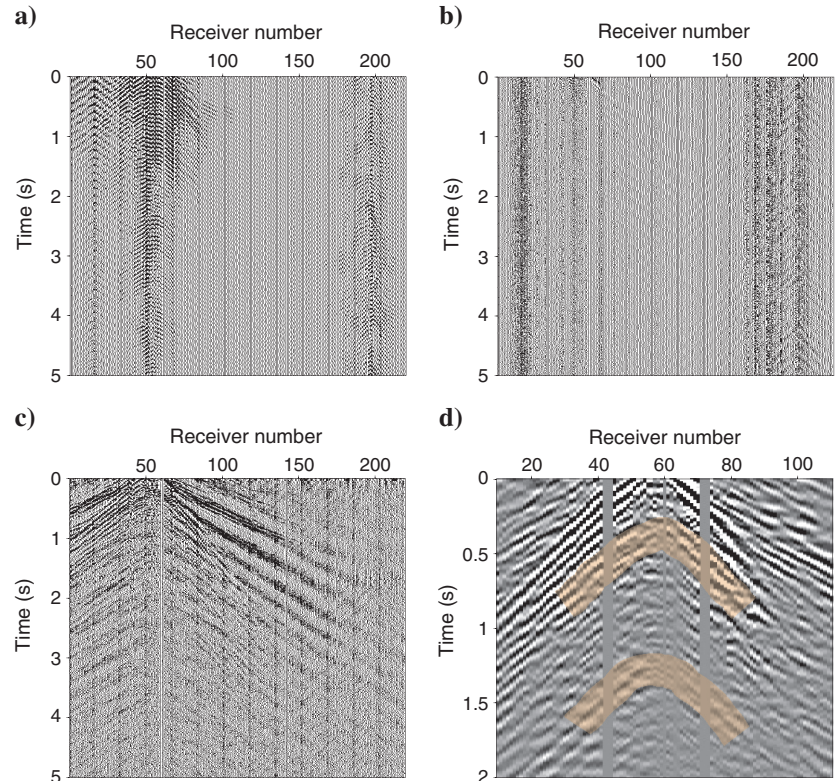


Figure 3. Virtual source gathers generated by (a) crosscorrelation, (b) deconvolution, and (c) cross-coherence. The pseudosource point of these gathers is at receiver number 60. We applied no filter to these displayed data. (d) Detail showing hyperbolic events of panel (c). The main hyperbolic events are highlighted in transparent yellow. A band-pass filter and f - k filter have been applied to the data in panel (d). The data gaps in panel (d) are caused by the removal of incoherent traces.

quasi-linear, paralleling the river; several roads and railways were crossed by or run parallel to the line (shown by solid arrows in Figure 2a). It might appear that the sparsity of roads and railways does not provide an adequate illumination, but, as shown in Figure 1, the number of stationary points increases dramatically when one considers multiples that are reflected from different reflectors. The length of the survey line is about 2180 m, with single-horizontal-component geophones oriented orthogonal to the survey line at 10-m intervals aimed at obtaining subsurface structure from shear wave data. We use analog-to-digital converter DSS-12 (Suncoch Consultants) to digitize and store traffic noise. The data were stored in 1200 time windows of 30-s duration, at a 4-ms sampling interval. Figure 2b shows an example of a noise record along the entire line. Higher levels of traffic noise originated from roads and railways that cross the survey line at receiver numbers 20, 50, 180, and 200. The source wavelets for the traffic noise had wide-ranging and complex frequency spectra because much of the traffic ran continuously, with differing characteristics attributable to the varying speed or weight of the vehicles. Frequency analysis reveals that the most energetic part of traffic noise is in the range 12–16 Hz (Figure 2c).

Figures 3a–3c compare the pseudoshot gathers derived from crosscorrelation, deconvolution, and cross-coherence. We add white noise, which has a 3% amplitude of the average power spectrum of the pseudosource trace in deconvolution and a 0.01% amplitude of the average amplitude of the denominator in equation 7 in cross-coherence in the frequency-domain. We find empirically that these

values are the smallest values that provide stable pseudoshot gathers. Because we used transverse geophones, these shot gathers are dominated by shear waves. For each of the three different operations, the data acquired at receiver point 60 is used as the reference trace. The interferometric data from the 1200 records are stacked, and no other filter is applied to the records to construct these interferometry profiles. In the crosscorrelation result (Figure 3a), ringing noise is dominant because of the periodic characteristic of the source wavelets of the noise generated by trains and trucks, and amplitude levels are particularly high at positions near the traffic noise sources (receiver numbers 20, 50, 180, and 200). While the ringing noise is suppressed in the deconvolution shown in Figure 3b, the signal-to-noise ratio is low, and large local amplitude variations remain. Of these methods, for reasons explained below, cross-coherence (Figure 3c) gives the best results in terms of both signal-to-noise ratio and trace balance. This virtual source record exhibits reflected shear waves with hyperbolic moveouts of the events particularly around 0.4 and 1.3 s (highlighted in Figure 3d). Figure 3d shows events with nonhyperbolic moveouts, such as the direct P-wave, that do not correspond to a virtual shear-wave source at receiver number 60. These are likely to be artifacts of an imperfect location distribution of noise sources. These events are, however, suppressed by the NMO correction and the common midpoint (CMP) stack.

Reflection profiles from body waves

We perform seismic reflection data processing using the CMP stack method and apply time migration to the data sets from each of the three methods. CMPs are numbered by the location of the receivers along the acquisition line, consistent with the numbering in Figure 2a. After generating pseudoshot gathers by each interferometry method, we apply identical steps of band-pass filtering (5–35 Hz), f - k filtering (to reject surface-waves with velocities outside the range 250–2500 m/s), NMO correction by the root-mean-square (rms) velocity obtained from cross-coherence, CMP stack, time migration, and depth conversion. We determine the stacking velocity by performing constant-velocity stacks on NMO-corrected CMP gathers (Yilmaz et al., 2001; Stucchi and Mazzotti, 2009). Figure 4 displays a CMP gather at the CMP number 60 corrected with three different constant values of moveout velocity; highlighted areas in Figure 4a show the time intervals used for determining the stacking velocity. As shown in Figure 4b, the reflection arrival at around 0.43 s is flattened for an rms velocity between 680 and 880 m/s. Given the noise level in this figure, it is difficult to estimate the stacking velocity with great accuracy. The panels in Figure 4b and the corresponding range of rms velocity (680–880 m/s) suggest an uncertainty of perhaps 100 m/s. The interval-velocity structure obtained from the rms velocity function estimated by cross-coherence interferometry is shown with the black line in Figure 5d. Figure 6a–6c shows the migrated depth sections using all pseudoshot records derived through crosscorrelation, deconvolution, and cross-coherence, respectively. We applied the same shear wave stacking velocity function to the recorded active-shot data.

In the image obtained from crosscorrelation (Figure 6a), anomalously strong waves dominate the image. These are caused by strong vibrations generated by the crossing traffic. This result agrees with the results obtained by Hohl and Mateeva (2006), whose image is also contaminated by local strong waves induced

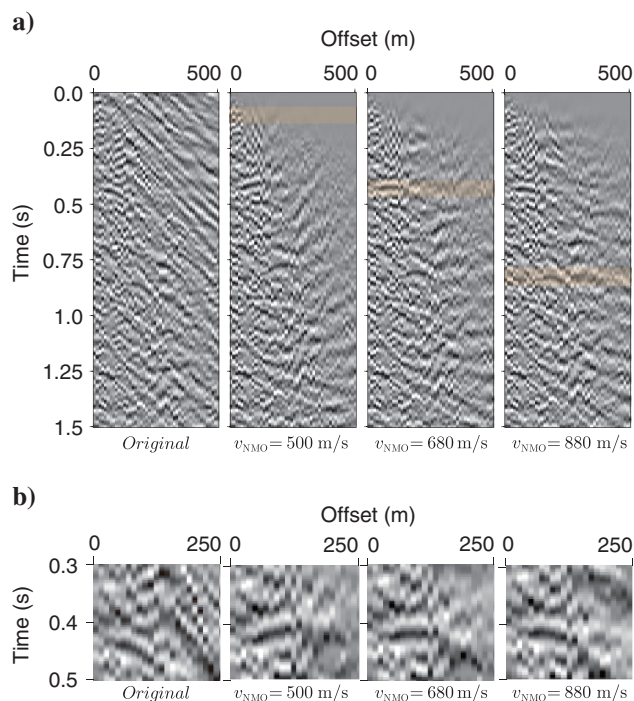


Figure 4. Constant-velocity NMO-corrected CMP gathers at the CMP number 60. (a) The leftmost panel is the original gather, and the other three panels are gathers corrected using the NMO velocity shown below each panel. The highlighted areas show the time intervals within which the rms velocity best flattens the local reflection. (b) Detailed views of the CMP gathers highlighting the reflection event at about 0.4 s.

by rig activity. The image in Figure 6a displays a marked periodicity; this is due to the narrow-band character of the noise sources (trucks and trains). As shown in Figure 3a, the crosscorrelation does not compensate for the narrow-band properties of the noise sources. The image retrieved by deconvolution (Figure 6b) is also noisy, although the amplitude is less variable from one location to another. The image in Figure 6b is noisy and incoherent. This is due to the fact that the virtual source gathers obtained by deconvolution interferometry (e.g., Figure 3b) show few coherent arrivals. Cross-coherence interferometry gives by far the clearest image of the three methods (Figure 6c). Because cross-coherence interferometry flattens the power spectrum via the normalization in the frequency-domain, this type of interferometry gives an image that contains a much larger range of spatial wavenumbers than the image obtained from cross-correlation (Figure 6a).

For comparison, we show in Figure 6d a conventional stacked and migrated reflection seismic section using 224 transverse active seismic sources, which are at approximately 10-m intervals along the receiver line and recorded by transverse-component geophones along the same line. Because, for practical reasons, it is not possible to deploy sources close to the receiver line in the active-shot experiments, the structure shallower than about 50 m is not imaged well in Figure 6d. In contrast, shallow reflections are evident in the seismic section of Figure 6c obtained from cross-coherence interferometry. Although we apply the same band-pass filter, the images in Figures 6c and 6d have different depth resolutions because of the different frequency content of the sources. Images from reflected shear waves are usually noisier than P-wave images, and the images obtained from traffic noise (Figure 6c) and from active shots (Figure 6d) are both contaminated with noise. Yet both images show coherent layered structures with a region of large reflectivity between receivers 80 and 140.

Delineation of structures shallower than 300 m in Figure 6c is useful not only for geophysical exploration, e.g., static corrections and near-surface tomography, but also for ground-motion prediction by seismic monitoring in earthquake disaster prevention and basement surveys in civil-engineering applications. Although trace-to-trace amplitudes are not preserved in the cross-coherence method, the method can still be used for the delineation of underground structures.

S-wave velocity from surface-waves

We apply the cross-coherence interferometry technique to a shear wave velocity estimation from the retrieved Love waves. The virtual shot record from cross-coherence interferometry (Figure 5a) clearly displays surface-waves. Figures 5b and 5c show the frequency-dependent phase velocity and dispersion curve estimated from the pseudoshot record at receiver number 190.

We pick the phase velocity of the fundamental mode Love wave (blue crosses in Figure 5c)

and use these measurements to invert for the shear-velocity as a function of depth using a genetic algorithm (Saito and Kabasawa, 1993; Yamanaka and Ishida, 1995; Hayashi, 2008). The inverted shear-velocity model is shown by the red line in Figure 5c. The shear wave interval-velocity distribution down to around 300 m obtained from the phase velocity measurements is shown by the red line in Figure 5d. This shear-velocity profile agrees well with the interval-velocity profile obtained from NMO correction of the reflected shear waves (black line in Figure 5d). The shallow part of the shear-velocity profile from the surface-wave analysis resolves several layers, with gradually changing velocity. This shear wave interval-velocity, obtained by cross-coherence interferometry of traffic noise, is useful for estimating and monitoring ground soil strength.

ERROR PROPAGATION

In this section, we compare the statistical properties of cross-coherence with those of cross-correlation and deconvolution, and show, theoretically, why cross-coherence is preferable in the data applications shown in this work.

Correction of amplitude variation among traces

Consider the processing of data whose amplitudes vary trace by trace as a result of variations in source strength and differences in the positioning or sensitivity of receivers. Ideally, the sensitivity is

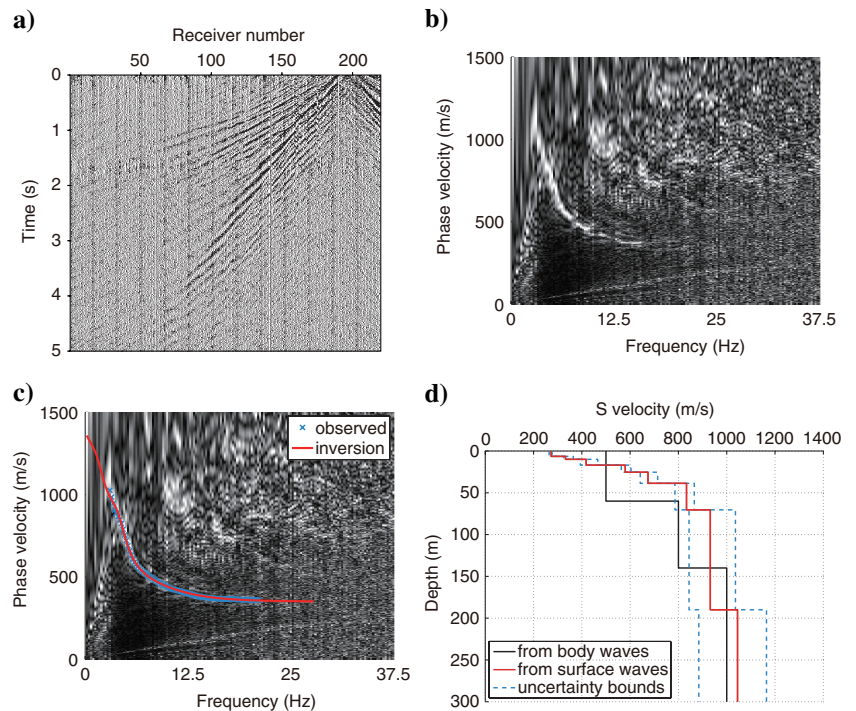


Figure 5. (a) Pseudoshot gather obtained by cross-coherence interferometry for a virtual source at receiver number 190. (b) Frequency-dependent phase velocity. (c) Dispersion curve overlaying the phase velocity plot (b). (d) Interval-velocity computed by inversion of the data in panel (c). In panel (c), the blue x's show the picking points for the fundamental mode of the surface-wave, and the red line is the dispersion curve obtained from inversion. The black line in (d) is the interval-velocity function obtained from the rms velocity profile used in the CMP stack of the reflected transverse waves, the red line is the estimated shear wave velocity, and the blue dashed lines show an estimate of the uncertainty resulting from the uncertainty in the phase velocity picks in (c).

the same for all receivers, but in practice this is not the case because of variations in ground coupling and local topography. The equations of the three methods are

$$C_{A\alpha} = u(r_A, s)u^*(r_\alpha, s), \quad (8)$$

$$D_{A\alpha} = \frac{u(r_A, s)u^*(r_\alpha, s)}{|u(r_\alpha, s)|^2}, \quad (9)$$

$$D_{\alpha A} = \frac{u(r_{\alpha, s})u^*(r_A, s)}{|u(r_A, s)|^2}, \quad (10)$$

$$H_{A\alpha} = \frac{u(r_A, s)u^*(r_\alpha, s)}{|u(r_A, s)||u(r_\alpha, s)|}, \quad (11)$$

where two receivers are at r_A and r_α . Deconvolution interferometry is asymmetric in that the amplitude of the extracted signal changes when we exchange the pseudosource and receiver points: this method thus has two different forms. Consider the case where receiver r_A records the average amplitude of all receivers and r_α records an anomalously large amplitude; the recorded motion at receiver r_A is $u(r_A, s) = G(r_A, s)$, and the motion recorded at r_α is $u(r_\alpha, s) = RG(r_\alpha, s)$ with $R \gg 1$, an amplification factor. The amplitude of the

signals extracted with crosscorrelation and cross-coherence does not change by exchanging α and A .

Let us compare the amplitudes among equations 8–11. In equation 8, $C_{A\alpha} = RG(r_A, s)G^*(r_\alpha, s)$, and the amplitude of $C_{A\alpha}$ is thus amplified by a factor R . Similarly, the amplitudes of $D_{A\alpha}$ and $D_{\alpha A}$ are multiplied by $1/R$ and R , respectively. As mentioned above, the amplitudes of $C_{A\alpha}$, $D_{A\alpha}$, and $D_{\alpha A}$ differ from the average amplitude. Accordingly, in an analysis based on crosscorrelation or deconvolution that includes the anomalous receiver α , the amplitude of the extracted response is unbalanced, thus requiring the additional task of removing these variations. The amplitude of $H_{A\alpha}$ is 1, independent of R . That is, cross-coherence removes the influence of amplitude variations and achieves a stable amplitude without separate processing to normalize the amplitude of traces constructed by interferometry.

The influence of additive noise

When the data are contaminated by additive random noise $N(r)$ with zero mean, the wavefield $u(r_A, s)$ includes a noise term $N(r_A)$,

$$u(r_A, s) = W(s)G(r_A, s) + N(r_A). \quad (12)$$

For simplicity, let us set the source signature $|W(s)| = 1$. This additive noise might be caused by microtremors, electric noise in the equipment, and human activities. Henceforth, we abbreviate $G(r_A, s)$ as G_A , $N(r_A, s)$ as N_A , and $W(s)$ as W . In Appendix A,

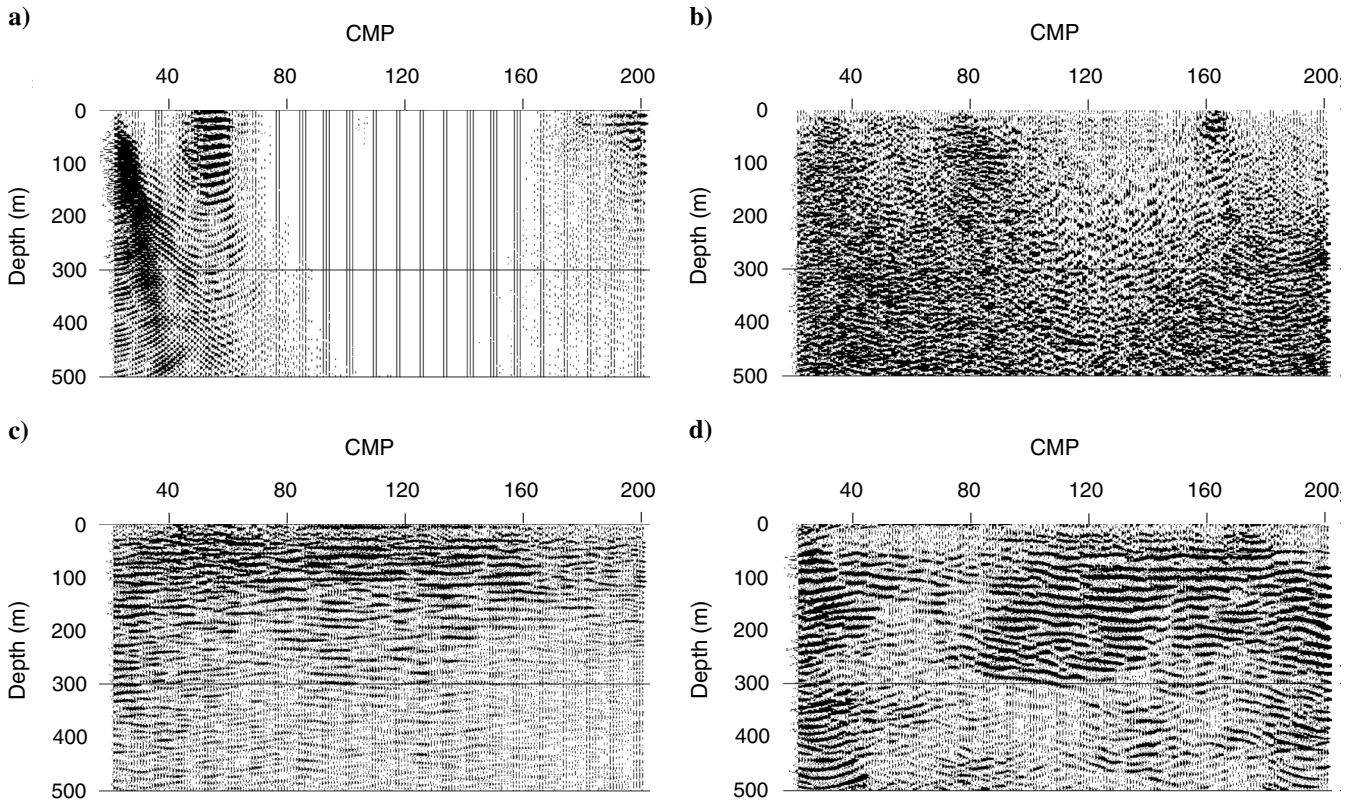


Figure 6. Subsurface structure obtained by CMP stack, time migration, and depth conversion using reflected waves obtained by (a) cross-correlation, (b) deconvolution, and (c) cross-coherence interferometry. Panel (d) is generated from active-source data. A band-pass filter between 5 and 35 Hz has been applied to all the data before imaging.

we insert equation 12 into equations 2, 4, and 5 and expand in the small quantity $|N|/|G| < 1$.

To investigate the influence of additive noise, we take the ensemble average to estimate the mean and variance of equations A-8–A-10 (Appendix A). Because the ensemble average of random noise is assumed to vanish, the ensemble average of the convolution of G and N also vanishes. As shown in the equations A-8–A-10, the ensemble average values of the crosscorrelation, deconvolution, and cross-coherence in the presence of additive noise are thus given by

$$\langle C_{AB} \rangle = G_A G_B^*, \quad (13)$$

$$\langle D_{AB} \rangle = \frac{G_A G_B^*}{|G_B|^2}, \quad (14)$$

$$\langle H_{AB} \rangle = \left(1 - \frac{1}{4} \frac{|N_A|^2}{|G_A|^2} - \frac{1}{4} \frac{|N_B|^2}{|G_B|^2} \right) \frac{G_A G_B^*}{|G_A| |G_B|}, \quad (15)$$

in which “ $\langle \rangle$ ” indicates an ensemble average. Their variances are

$$\sigma_C^2 = |G_B|^2 \sigma_{N_A}^2 + |G_A|^2 \sigma_{N_B}^2, \quad (16)$$

$$\sigma_D^2 = \frac{1}{|G_B|^2} \sigma_{N_A}^2 + \frac{|G_A|^2}{|G_B|^4} \sigma_{N_B}^2, \quad (17)$$

$$\sigma_H^2 = \frac{1}{2|G_A|^2} \sigma_{N_A}^2 + \frac{1}{2|G_B|^2} \sigma_{N_B}^2. \quad (18)$$

Here σ_N denotes a standard deviation of the additive noise. Note that the noise does not bias the ensemble average of the crosscorrelation and the deconvolution (equations 13 and 14), but according to expression 15 it does lead to a bias in the cross-coherence. Therefore, when we stack many times to mimic an ensemble average, the influence of noise remains as a bias in the cross-coherence. Because, however, the cross-coherence does not preserve amplitude even in the absence of noise, the multiplicative bias in equation 15 is of little concern in practice.

It is difficult to compare the variances in equations 16, 17, and 18 because they express the variance in different quantities (cross-correlation, deconvolution, and cross-coherence, respectively). Instead, we consider the normalized standard deviations

$$\frac{\sigma_C}{|C_{AB}|} = \sqrt{\frac{\sigma_{N_A}^2}{|G_A|^2} + \frac{\sigma_{N_B}^2}{|G_B|^2}}, \quad (19)$$

$$\frac{\sigma_D}{|D_{AB}|} = \sqrt{\frac{\sigma_{N_A}^2}{|G_A|^2} + \frac{\sigma_{N_B}^2}{|G_B|^2}}, \quad (20)$$

$$\frac{\sigma_H}{|H_{AB}|} = \sqrt{\frac{\sigma_{N_A}^2}{2|G_A|^2} + \frac{\sigma_{N_B}^2}{2|G_B|^2}}. \quad (21)$$

From equations 19–21, the normalized standard deviations are related as follows:

$$\frac{\sigma_H}{|H_{AB}|} = \frac{1}{\sqrt{2}} \frac{\sigma_C}{|C_{AB}|} = \frac{1}{\sqrt{2}} \frac{\sigma_D}{|D_{AB}|}. \quad (22)$$

As shown in equation 22, the relative uncertainty in the cross-coherence is about 70% of that of the other methods.

In summary, additive random noise causes an inconsequential bias in the cross-coherence, but the relative statistical uncertainty in the cross-coherence is reduced by a factor $1/\sqrt{2}$ ($\approx 70\%$) compared with that of crosscorrelation and deconvolution. Thus, in addition to treating the problem of anomalous trace amplitudes, cross-coherence is more stable in the presence of noise.

We study the influence of additive random noise by a numerical example of synthetic data generated by a two-dimensional acoustic finite-difference time domain method with a model consisting of two horizontal constant-density layers (Figure 7). The virtual source sections, obtained from the noise-contaminated traces and shown in Figure 8, display the direct arrival, which is represented with the dashed arrow in Figure 7 at 1.3 s, and the reflected wave, which is depicted by the thick arrow in Figure 7 at 2.5 s. The leftmost trace in each plot is noise-free so the signal-to-noise ratio is infinite. The signal-to-noise ratio (calculated from the maximum amplitude of direct arrival) of the second trace from the left is 20, which means that we added 5% random noise, whereas that of the third trace is 19, and that of the fourth trace is 18. The amount of noise gradually increases until the rightmost trace, whose signal-to-noise ratio is one. Figure 8a, 8b, and 8c shows the wavefields retrieved from crosscorrelation, deconvolution, and cross-coherence, respectively. Because the amplitudes are not preserved in either of our processing schemes, and because the crosscorrelation has a different physical dimension than the deconvolution and cross-coherence, one cannot compare absolute amplitudes in Figure 8a, 8b, and 8c. What is relevant, though, is the signal-to-noise ratio in these figures. For low signal-to-noise ratios, the direct and reflected waves are buried in ambient noise in both the crosscorrelation and deconvolution results

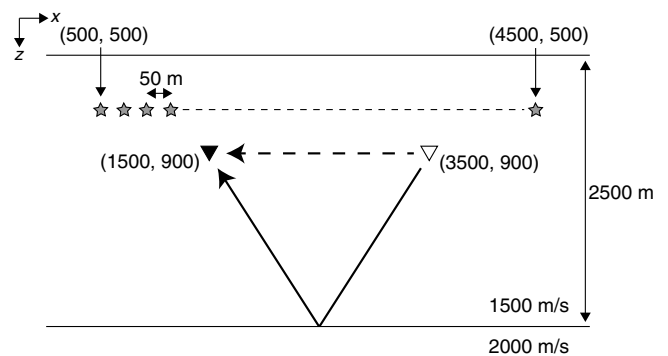


Figure 7. Two horizontal constant-density layers model, with an interface at 2500-m depth. The velocities of the layers are 1500 and 2000 m/s, respectively. Two receivers, which are shown with triangles, are positioned at 900-m depth and at lateral positions $x = 1500$ and 3500 m. Dashed and thick arrows denote, respectively, a direct and a reflected wavefield created by interferometry. The sources, which are represented by stars, are distributed in a horizontal line at 500-m depth, ranging from $x = 500$ to 4500 m, in increments of 50 m.

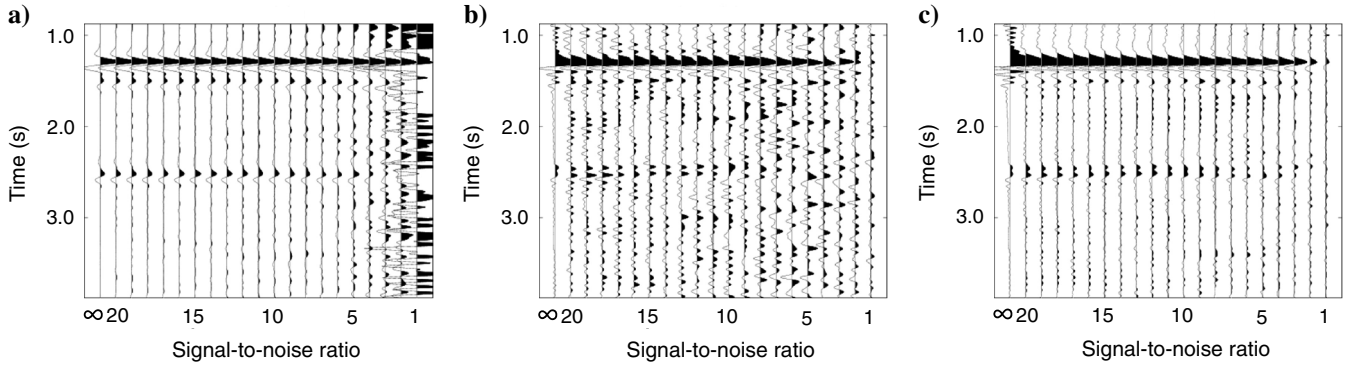


Figure 8. The influence of random noise added to the simulation data before applying (a) crosscorrelation, (b) deconvolution, and (c) cross-coherence interferometry. In each figure, the signal-to-noise ratio varies between traces. No noise is added to the leftmost trace. The second trace from the left has a signal-to-noise ratio of 20, the signal-to-noise ratio is decreased by one for each successive trace. The signal-to-noise ratio of the rightmost trace is one. Because the amplitude is not preserved in either of the processing schemes, the absolute amplitude cannot be relevant, but the signal-to-noise ratios in the different panels can be compared.

(Figure 8a and 8b). In contrast, cross-coherence interferometry (Figure 8c) reduces the influence of ambient noise.

CONCLUSION

In our study, cross-coherence interferometry provided the clearest pseudoshot gathers generated from highly variable and strong traffic noise and retrieved both reflected shear waves and Love waves. Because we used recordings of the transverse motion, this procedure yielded virtual source gathers for shear waves. The imprint of the source signature and amplitude variations between receivers is suppressed in the virtual source gathers obtained from cross-coherence. They provide shear wave images obtained by migrating virtual source data that agree to a large extent with those obtained with active sources. Moreover, the images obtained by active sources lack the shallow structures seen in the image obtained from the cross-coherence of traffic noise, because the active sources were placed at a distance from the survey line. The virtual source sections obtained from cross-coherence exhibit both surface-waves and body waves; we used the surface-wave data to carry out dispersion measurements of the fundamental mode Love waves and obtained a shear wave velocity profile that agrees with the interval-velocity function calculated by the stacking velocity profile. Corresponding with early studies, it is easier to extract surface-waves than body waves.

Compared with the standard deviation of the virtual source sections obtained from crosscorrelation and deconvolution, the relative statistical uncertainty in cross-coherence is 30% lower. In contrast to crosscorrelation and deconvolution, additive noise leads to a multiplicative bias in virtual source signals based on cross-coherence. Because the cross-coherence method does not conserve trace-to-trace amplitude, this multiplicative bias is of little concern. Because of the normalization employed, the method overcomes amplitude variations among traces. In any case, because the amplitude information is lost, cross-coherence interferometry is inappropriate for data analysis that exploits amplitude information, such as the measurement of reflection coefficients, amplitude variation with offset, and attenuation. Cross-coherence is particularly suitable for data that are noisy, vary in amplitude among traces, or have long and complex source wavelets. The primary target of cross-coherence interferometry here is the estimation of shear wave

velocity from surface-waves and the shape of subsurface structures obtained from reflected body waves. By using the transverse-component of the ground motion for cross-coherence, we obtain a shear-velocity profile and a shear wave image of the subsurface. This information is useful for various applications, such as static corrections, near-surface tomography, ground motion prediction for earthquake disaster prevention, monitoring the ground soil strength, and basement surveys for civil engineering.

ACKNOWLEDGMENTS

We are grateful to Kyosuke Onishi of Akita University, Toshiyuki Kurahashi of Public Works Research Institute, and Takao Aizawa of Suncoh Consultants for the acquisition of the seismic data and Tatsunori Ikeda of Kyoto University for the technical support in surface-wave analysis. We also thank Akihisa Takahashi of JGI, Inc., Shohei Minato of Kyoto University, the editor, and three anonymous reviewers for suggestions, corrections, and discussions. Norimitsu Nakata is grateful for support from the Japan Society for the Promotion of Science (JSPS: 22-5857).

APPENDIX A

ERROR PROPAGATION

By substituting equation 12 into equations 2, 4, and 5, and assuming that $|W(s)| = 1$, we obtain the following expressions for cross-correlation, deconvolution, and cross-coherence using wavefields that include random noise with zero mean

$$C_{AB} = (WG_A + N_A)(W^*G_B^* + N_B^*), \quad (\text{A-1})$$

$$D_{AB} = \frac{WG_A + N_A}{WG_B + N_B}, \quad (\text{A-2})$$

$$H_{AB} = \frac{(WG_A + N_A)(W^*G_B^* + N_B^*)}{|WG_A + N_A||WG_B + N_B|}. \quad (\text{A-3})$$

Below, we assume that the additive noise at different locations is uncorrelated; hence

$$\langle |N_A|^2 \rangle = \sigma_{N_A}^2, \quad \langle |N_B|^2 \rangle = \sigma_{N_B}^2, \quad \langle N_A N_B^* \rangle = 0. \quad (\text{A-4})$$

When ψ represents the phase,

$$N = |N|e^{i\psi}, \quad (\text{A-5})$$

then under the assumption that the amplitude and phase are uncorrelated, the ensemble average of N^2 is

$$\langle N^2 \rangle = \langle |N|^2 e^{2i\psi} \rangle = \langle |N|^2 \rangle \langle e^{2i\psi} \rangle. \quad (\text{A-6})$$

We assume that the phase has a uniform distribution, thus $\langle e^{2i\psi} \rangle = 0$, hence

$$\langle N_A^2 \rangle = \langle N_B^2 \rangle = 0. \quad (\text{A-7})$$

We further assume that the level of additive noise is small ($|N|/|G| < 1$) and expand equations A-1–A-3 in $|N|/|G|$. Ignoring noise terms higher than second-order in $|N|/|G|$, gives

$$C_{AB} = G_A G_B^* + W^* N_A G_B^* + W G_A N_B^* + N_A N_B^* \quad (\text{A-8})$$

$$D_{AB} = \frac{G_A G_B^*}{|G_B|^2} + \frac{W^* N_A G_B^*}{|G_B|^2} - \frac{W^* G_A G_B^* N_B G_B^*}{|G_B|^4} - \frac{(W^*)^2 N_A G_B^* N_B G_B^*}{|G_B|^4} + \frac{(W^*)^2 G_A G_B^* N_B G_B^* N_B G_B^*}{|G_B|^6} \quad (\text{A-9})$$

$$H_{AB} = \left(1 - \frac{1}{4} \frac{|N_A|^2}{|G_A|^2} - \frac{1}{4} \frac{|N_B|^2}{|G_B|^2} \right) \frac{G_A G_B^*}{|G_A| |G_B|} + \frac{1}{2} \frac{W^* N_A G_B^*}{|G_A| |G_B|} + \frac{1}{2} \frac{W G_A N_B^*}{|G_A| |G_B|} + \frac{1}{4} \frac{N_A N_B^*}{|G_A| |G_B|} - \frac{1}{2} \frac{W G_A G_B^* G_A N_A^*}{|G_A|^3 |G_B|} - \frac{1}{2} \frac{W^* G_A G_B^* N_B G_B^*}{|G_A| |G_B|^3} - \frac{1}{8} \frac{(W^*)^2 N_A G_A^* N_A G_B^*}{|G_A|^3 |G_B|} - \frac{1}{8} \frac{W^2 G_A N_B^* G_B N_B^*}{|G_A| |G_B|^3} - \frac{1}{4} \frac{W^2 G_A N_A^* G_A N_B^*}{|G_A|^3 |G_B|} - \frac{1}{4} \frac{(W^*)^2 N_A G_B^* N_B G_B^*}{|G_A| |G_B|^3} + \frac{3}{8} \frac{W^2 G_A G_B^* G_A N_A^* G_A N_A^*}{|G_A|^5 |G_B|} + \frac{3}{8} \frac{(W^*)^2 G_A G_B^* N_B G_B^* N_B G_B^*}{|G_A| |G_B|^5} + \frac{1}{4} \frac{G_A G_B^* G_A N_A^* N_B G_B^*}{|G_A|^3 |G_B|^3}. \quad (\text{A-10})$$

Taking expectation values gives the mean and variance of equations 13–18.

REFERENCES

Aki, K., 1957, Space and time spectra of stationary stochastic waves, with special reference to microtremors.: Bulletin of the Earthquake Research Institute, University of Tokyo, **35**, 415–456.

- Bakulin, A., and R. Calvert, 2004, Virtual source: New method for imaging and 4D below complex overburden: 74th Annual International Meeting, SEG, Expanded Abstracts, **23**, 112–115.
- Bendat, J., and A. Piersol, 2000, Random data: Analysis and measurement procedures: John Wiley & Sons.
- Bensen, G. D., M. H. Ritzwoller, M. P. Barmin, A. L. Levshin, F. Lin, M. P. Moschetti, N. M. Shapiro, and Y. Yang, 2007, Processing seismic ambient noise data to obtain reliable broad-band surface-wave dispersion measurements: Geophysical Journal International, **169**, 1239–1260, doi: [10.1111/gji.2007.169.issue-3](https://doi.org/10.1111/gji.2007.169.issue-3).
- Campillo, M., and A. Paul, 2003, Long-range correlations in the diffuse seismic coda: Science, **299**, 547–549, doi: [10.1126/science.1078551](https://doi.org/10.1126/science.1078551).
- Chávez-García, F. J., and F. Luzón, 2005, On the correlation of seismic microtremors: Journal of Geophysical Research, **110**, B11313, doi: [10.1029/2005JB003671](https://doi.org/10.1029/2005JB003671).
- Claerbout, J. F., 1968, Synthesis of a layered medium from its acoustic transmission response: Geophysics, **33**, 264–269, doi: [10.1190/1.1439927](https://doi.org/10.1190/1.1439927).
- Draganov, D., X. Campman, J. Thorbecke, A. Verdel, and K. Wapenaar, 2009, Reflection images from ambient seismic noise: Geophysics, **74**, no. 5, A63–A67, doi: [10.1190/1.3193529](https://doi.org/10.1190/1.3193529).
- Draganov, D., K. Wapenaar, W. Mulder, J. Singer, and A. Verdel, 2007, Retrieval of reflections from seismic background-noise measurements: Geophysical Research Letters, **34**, L04305, doi: [10.1029/2006GL028735](https://doi.org/10.1029/2006GL028735).
- Gerstoft, P., P. Shearer, N. Harmon, and J. Zhang, 2008, Global P, PP, and PKP wave microseisms observed from distant storms: Geophysical Research Letters, **35**, L23306, doi: [10.1029/2008GL036111](https://doi.org/10.1029/2008GL036111).
- Hayashi, K., 2008, Development of surface-wave methods and its application to site investigations: Ph.D. thesis, Kyoto University.
- Hohl, D., and A. Mateeva, 2006, Passive seismic reflectivity imaging with ocean-bottom cable data: 76th Annual International Meeting, SEG, Expanded Abstracts, **25**, 1560–1564.
- Lobkis, O. I., and R. L. Weaver, 2001, On the emergence of the Green's function in the correlations of a diffuse field: Journal of the Acoustical Society of America, **110**, 3011–3017, doi: [10.1121/1.1417528](https://doi.org/10.1121/1.1417528).
- Miyazawa, M., R. Snieder, and A. Venkataraman, 2008, Application of seismic interferometry to extract P- and S-wave propagation and observation of shear-wave splitting from noise data at Cold Lake, Alberta, Canada: Geophysics, **73**, no. 4, D35–D40, doi: [10.1190/1.2937172](https://doi.org/10.1190/1.2937172).
- Nakata, N., 2010, Virtual world in geophysics; synthesized data by interferometry and simulation: M.Sc. thesis, Kyoto University.
- O'Connell, D. R. H., 2007, Concrete dams as seismic imaging sources: Geophysical Research Letters, **34**, L20307, doi: [10.1029/2007GL031219](https://doi.org/10.1029/2007GL031219).
- Prieto, G. A., J. F. Lawrence, and G. C. Beroza, 2009, Anelastic earth structure from the coherency of the ambient seismic field: Journal of Geophysical Research, **114**, B07303, doi: [10.1029/2008JB006067](https://doi.org/10.1029/2008JB006067).
- Roux, P., and M. Fink, 2003, Green's function estimation using secondary sources in a shallow wave environment: Journal of the Acoustical Society of America, **113**, 1406–1416, doi: [10.1121/1.1542645](https://doi.org/10.1121/1.1542645).
- Roux, P., K. Sabra, P. Gerstoft, and W. Kuperman, 2005, P-waves from crosscorrelation of seismic noise: Geophysical Research Letters, **32**, L19303, doi: [10.1029/2005GL023803](https://doi.org/10.1029/2005GL023803).
- Saito, M., and H. Kabasawa, 1993, Computations of reflectivity and surface-wave dispersion curves for layered media ii. Rayleigh wave calculations: Butsuri-Tansa, **46**, 283–298.
- Schuster, G. T., J. Yu, J. Sheng, and J. Rickett, 2004, Interferometric/daylight seismic imaging: Geophysical Journal International, **157**, 838–852, doi: [10.1111/gji.2004.157.issue-2](https://doi.org/10.1111/gji.2004.157.issue-2).
- Shapiro, N. M., M. Campillo, L. Stehly, and M. H. Ritzwoller, 2005, High-resolution surface-wave tomography from ambient seismic noise: Science, **307**, 1615–1618, doi: [10.1126/science.1108339](https://doi.org/10.1126/science.1108339).
- Snieder, R., 2004, Extracting the Green's function from the correlation of coda waves: A derivation based on stationary phase: Physical Review E, **69**, 046610, doi: [10.1103/PhysRevE.69.046610](https://doi.org/10.1103/PhysRevE.69.046610).
- Snieder, R., M. Miyazawa, E. Slob, I. Vasconcelos, and K. Wapenaar, 2009, A comparison of strategies for seismic interferometry: Surveys in Geophysics, **30**, 503–523.
- Snieder, R., and E. Şafak, 2006, Extracting the building response using seismic interferometry: Theory and application to the Millikan library in Pasadena, California: Bulletin of the Seismological Society of America, **96**, 586–598, doi: [10.1785/0120050109](https://doi.org/10.1785/0120050109).
- Snieder, R., K. Wapenaar, and K. Larner, 2006, Spurious multiples in seismic interferometry of primaries: Geophysics, **71**, no. 4, S1111–S1124, doi: [10.1190/1.2211507](https://doi.org/10.1190/1.2211507).
- Stucchi, E., and A. Mazzotti, 2009, 2D seismic exploration of the Ancona landslide (Adriatic Coast, Italy): Geophysics, **74**, no. 5, B139–B151, doi: [10.1190/1.3157461](https://doi.org/10.1190/1.3157461).
- Vasconcelos, I., and R. Snieder, 2008a, Interferometry by deconvolution: Part I — Theory for acoustic waves and numerical examples: Geophysics, **73**, no. 3, S115–S128, doi: [10.1190/1.2904554](https://doi.org/10.1190/1.2904554).

- Vasconcelos, I., and R. Snieder, 2008b, Interferometry by deconvolution: Part 2 — Theory for elastic waves and application to drill-bit seismic imaging: *Geophysics*, **73**, no. 3, S129–S141, doi: [10.1190/1.2904985](https://doi.org/10.1190/1.2904985).
- Vasconcelos, I., R. Snieder, and B. Hornby, 2008, Imaging internal multiples from subsalt VSP data — Examples of target-oriented interferometry: *Geophysics*, **73**, no. 4, S157–S168, doi: [10.1190/1.2944168](https://doi.org/10.1190/1.2944168).
- Wapenaar, K., 2003, Synthesis of an inhomogeneous medium from its acoustic transmission response: *Geophysics*, **68**, 1756–1759, doi: [10.1190/1.1620649](https://doi.org/10.1190/1.1620649).
- Wapenaar, K., 2004, Retrieving the elastodynamic Green's function of an arbitrary inhomogeneous medium by crosscorrelation: *Physical Review Letters*, **93**, 254–301, doi: [10.1103/PhysRevLett.93.254301](https://doi.org/10.1103/PhysRevLett.93.254301).
- Wapenaar, K., D. Draganov, R. Snieder, X. Campman, and A. Verdel, 2010, Tutorial on seismic interferometry: Part 1 — Basic principles and applications: *Geophysics*, **75**, no. 5, 75A195–75A209, doi: [10.1190/1.3457445](https://doi.org/10.1190/1.3457445).
- Wapenaar, K., and J. Fokkema, 2006, Green's function representations for seismic interferometry: *Geophysics*, **71**, no. 4, S133–S146, doi: [10.1190/1.2213955](https://doi.org/10.1190/1.2213955).
- Wapenaar, K., E. Slob, and R. Snieder, 2008a, Seismic and electromagnetic controlled-source interferometry in dissipative media: *Geophysical Prospecting*, **56**, 419–434, doi: [10.1111/j.1365-2478.2007.00686.x](https://doi.org/10.1111/j.1365-2478.2007.00686.x).
- Wapenaar, K., J. van der Neut, and E. Ruigrok, 2008b, Passive seismic interferometry by multidimensional deconvolution: *Geophysics*, **73**, no. 6, A51–A56, doi: [10.1190/1.2976118](https://doi.org/10.1190/1.2976118).
- Yamanaka, H., and H. Ishida, 1995, Phase velocity inversion using genetic algorithms: *Journal of Structural and Construction Engineering*, **468**, 9–17.
- Yilmaz, O., I. Tanir, C. Gregory, and F. Zhou, 2001, Interpretive imaging of seismic data: *The Leading Edge*, **20**, 132–144, doi: [10.1190/1.1438892](https://doi.org/10.1190/1.1438892).
- Zhang, J., P. Gerstoft, and P. Shearer, 2009, High-frequency P-wave seismic noise driven by ocean winds: *Geophysical Research Letters*, **36**, L09302, doi: [10.1029/2009GL037761](https://doi.org/10.1029/2009GL037761).